LEVEL III

①

⑥ Application of Solidification Theory to
Rapid Solidification Processing.

⑩ W. J. Boettinger, J. W. Cahn, S. R. Coriell,
J. R. Manning, and R. J. Schaefer
Metallurgy Division
Center for Materials Science
National Bureau of Standards
Washington, D.C.   20234   A094285

⑨ Semi-Annual Technical Report. / Oct 84-31 Mar 81,
Period Covered: October 1, 1980 to March 31, 1981
⑮ ARPA Order No. 3751

⑪ Report Issued: June 1981   ⑫ 65

"The views and conclusions contained in this
document are those of the authors and should
not be interpreted as representing the official
policies, either expressed or implied, of the
Defense Advanced Research Projects Agency or
the U.S. Government."

DTIC
SELECTED
SEP 24 1981
D

AD A104561

DTIC FILE COPY

387444   LB

81 6   25 010

Table of Contents

Application of Solidification Theory to

Rapid Solidification Processing

1. Technical Report Summary

This semi-annual technical report for ARPA Order 3751 covers the period
October 1, 1980 to March 31, 1981. Significant accomplishments during this
period include:

Theory

o   Related phase diagram features in Ag-Cu to amount of extended solid
    solubility possible from rapid solidification.

o   Predicted values of intercellular segregation in rapidly solidified
    alloys as a function of (1) solidification velocity and (2) amplitude
    of solidification interface instability.

Experiment

o   Measured microstructures in rapidly solidified Al-Ag alloys for
    comparison with interface stability theory.

o   Measured sequences of microstructures formed as solidification
    velocity was accelerated and copper concentration was varied in Pd-
    Cu-Si alloys.

These accomplishments extend previous results obtained at NBS on this
contract on

(1) Prediction of alloy phases and compositions obtainable through
     rapid solidification.

(2) Predictions for solidification velocity regimes which produce
     special microstructures, such as metallic glasses.

(3) Calculation of critical solidification velocities for eliminating
     or minimizing alloy segregation.

1

Task Objective

The objective of this work is to develop guidelines based on kinetic and thermodynamic solidification theory for prediction and control of rapid solidification processes. In particular, segregation effects and rules governing the formation of equilibrium and non-equilibrium phases, including metallic glasses, will be investigated. Areas where significant improvements in alloy properties can be produced by rapid solidification will be emphasized.

Technical Problem and General Methodology

Rapid solidification techniques make it possible to produce new types of materials having significantly better properties than conventionally processed materials. However, improved predictive techniques and control of rapid solidification processes are needed. The current studies are focussed on the science underlying areas where improved materials can be obtained in order to provide such prediction and control. This work is both theoretical and experimental.

Two major ways in which rapid solidification technology provides improved materials are:

1. **Production of alloys with new compositions, microstructures and phases.**

    For example, through extended solid solubility, formation of metallic glass, and new phase reaction sequences.

2. **Production of more homogeneous materials.**

    For example, through reducing or eliminating intercellular and interdendritic alloy segregation.

In the current work, the thermodynamic and kinetic processes which control production of these improved materials have been investigated. Significant

2

results have been obtained in each area 1 and 2 outlined above. These results have provided guidelines for the design of alloys, e.g., compositions and solidification velocities where segregation can be avoided, and indicated critical regimes for processing control, e.g., critical solidification velocities where metallic glass will be formed. Further work now underway can be expected to provide additional guidelines on allowed ranges of extended solid solubility and on intercellular alloy segregation under rapid solidification conditions.

These results and guidelines have been obtained by first extending conventional solidification theory and thermodymanics to rapid solidification conditions in order to determine the effects of rapid solidification alone, independent of possible non-equilibrium influences. This approach, which had not been seriously attempted by previous workers in this field, yielded accomplishments such as (1) prediction of maximum limits on extended solid solubility, (2) predictions for the growth velocity regimes which produce special microstructures, such as metallic glasses, in rapidly solidified alloys, and (3) calculations of critical solidification velocities for eliminating or minimizing alloy segregation effects. A more detailed list of accomplishments is provided on pages 4 to 6.

A second important step in the application of thermodynamic and kinetic principles to rapid solidification conditions requires the inclusion of non-equilibrium influences, such as (1) the effect that lack of equilibrium at a rapidly solidifying interface has on the distribution coefficient and hence on the alloy segregation, (2) the effect of acceleration or other changes in solidification velocity on alloy microstructures, including the importance of transients, and (3) the production of extended solid solubility by partitionless rapid solidification in a two-phase region of the phase diagram. These items are planned for future work.

1.   New Compositions, Microstructures and Phases

Extended Solid Solubility

o   Theoretically derived rules relating maximum enhanced solid solubility
     to phase diagram features.

o   Applied these rules to silicon alloys and found agreement with results
     reported in the literature.

o   Applied theory to Ag-Cu alloy system having retrograde solidus in
     phase diagram.

o   Experimentally achieved enhanced solid solubility from electron beam
     melting and resolidification in Ag-Cu alloys. These experiments
     use Ag-Cu as an example of a broad class of alloys with a
     retrograde solidus, where enhanced solubility must be caused by a
     solute trapping mechanism.

Glass Formation

o   Developed theory providing boundaries for the region in the phase
     diagram where partitionless solidification is thermodynamically
     forbidden. In this region, a two-phase structure must be created if
     crystallization is to occur.

o   Showed that, because diffusion processes are required to sort out
     the constitutents into two-phase eutectic microstructures in this
     region, eutectic crystallization velocities typically will not
     exceed 5 cm/s, making glass formation easy during rapid solidification.

o   Experimentally determined maximum crystallization velocity for Pd-Cu-Si two-phase eutectic alloy. The strikingly sharp transition from crystalline microstructure to metallic glass as the solidification rate was accelerated, verified the basic premise that growth rate control rather than nucleation control was the factor preventing crystallization.

o   Measured the sequences of microstructures formed as functions of composition and solidification velocity in Pd-Cu-Si alloys as the solidification velocity was increased and determined the composition dependence of the critical velocity for glass formation. Found a minimum in this velocity near 6 at.% Cu.

Alloy Phases

o   Calculated thermodynamic bounds on the degree of metastability that can be obtained from rapid solidification.

o   Developed techniques for utilizing equilibrium phase diagrams for estimation of rapid solidification effects.

o   Produced criteria for recognizing when rapid solidification has given a solid alloy that is closer to equilibrium than obtained by conventional solidification.

o   Developed general rules governing the sequences in which combinations of metastable phases can occur in multicomponent alloys.

2.   More Homogeneous Materials

Segregation Produced by Unstable Solidification Interfaces

o   Examined directional and anisotropic factors influencing solidification

interface stability and showed that, while cells and dendrites formed as a result of interface breakdown will follow crystallographic directions at moderate velocities, they instead will follow temperature gradient directions when velocities are sufficiently high.

o   Calculated as a function of solidification velocity the wavelength (cell-size) at which interface instability occurs.

o   Developed theory relating amount of intercellular segregation to solidification velocity, distribution coefficient and amplitude of interface instability. Calculated typical values for segregation in rapidly solidified alloys.

Interface Stability

o   Developed morphological stability theory to include effects that become important at high solidification velocities, including (1) surface tension effects and (2) local deviations from equilibrium at the solidification interface.

o   Showed that, contrary to the trends at slower velocities, plane front solidification becomes increasingly stable with increasing velocity at rapid solidification velocities. This implies that alloy segregation due to interface instability might be completely avoided at very rapid solidification velocities.

o   Experimentally, analyzed the microstructure in rapidly solidified Al-Ag alloys to allow comparison with predictions of morphological stability theory. The results indicate that more than local growth conditions need to be considered.

A more detailed report of accomplishments during the period October 1980-March 1981 on (1) measurements of enhanced solid solubility in Ag-Cu, (2) calculation of alloy segregation from a non-planar solidification interface, (3) electron beam melting and rapid resolidification studies in Al-Ag alloys, and (4) investigations of critical velocities for metallic glass formation are given in the section on Report of Technical Progress and Results, starting on page 9. Recently developed items on the above accomplishment list covering these topics are discussed more thoroughly in that section.

Plans and Implications for Future Work

Electron beam surface melting experiments are planned to provide known, controlled rapid solidification velocities in Ag-Cu alloys. In these experiments the transition from two-phase to single phase microstructure as a function of solidification velocity will be investigated. This work will test theories developed in the current work concerning extended solid solubility. Alloys of Ag containing between 10 and 40 at.% Cu will be electron beam surface melted to different depths to obtain various solidification velocities. Transmission electron microscopy, scanning transmission electron microscopy and x-ray analysis will be performed to document the solidification conditions for the onset of extended solubility, solute trapping, and inverse dendrite coring. This work is designed to provide improved control and prediction of rapid solidification processes producing extended solid solubility.

Theoretical work will be performed to calculate interface shapes and solute segregation during cellular growth of binary alloys. Experimental results on interface stability in electron beam surface melted Al-Ag alloys will be compared with theoretical predictions. Initial predictions to be checked will be those obtained from conventional solidification theory as

7

affected by rapid solidification velocities. If it appears that transient effects from acceleration of the solidification velocities, effects from large concentration gradients at a rapidly solidifying interface, or non-equilibrium processes at this interface are of major importance, these influences will need to be treated further. Calculations will be made for the two-dimensional steady-state heat flow for a stationary circular source or a moving line source as produced by rastering an electron beam or laser to cause melting and rapid resolidification. These calculations are necessary to determine solidification velocities in these experiments so that the results can be related to predicted interface stability and segregation effects.

Detailed studies of the relation of observed microstructures to growth velocities and temperature gradients will be made for Al-Ag alloys using several of the melting modes available with the electron beam. Of particular importance are the overall sequence of temperature gradient and growth velocity conditions experienced by the interface during solidification, which may result in the interface either passing into an unstable regime and then into a regime of absolute stability, or completely by-passing the unstable regime. Long-range plans call for study of residual stress effects in surface melted samples. Many of the cracks in surface melted samples appear to be the result of hot tearing. To make useful surface coatings, this type of cracking must be eliminated since it cannot be rectified by post-melt processing.

In the area of metallic glass formation, further studies will be made of critical solidification velocities and accompanying sequences of microstructures. General rules to describe the results that have been obtained will be considered, particularly concerning the effect of variations in alloy composition.

8

NBS members working on this project have been active in organizing a conference on Rapid Solidication Technology sponsored by COMAT, with major input from DARPA, to be held at the National Bureau of Standards, July 1-2, 1981. Also, NBS members will participate in the DARPA Materials Research Council discussions on rapid solidification, La Jolla, California, July 1981.

2.   Report of Technical Progress and Results

Enhanced Solid Solubility and Solute Trapping

One of the fundamental questions related to rapid solidification is the degree of dependence of the distribution coefficient on interface velocity (and consequently on interface undercooling). We have chosen to study these effects in Ag-Cu alloys because of two interesting features of these alloys. First, the phase diagram consists of a simple eutectic between the Ag-rich and Cu-rich f.c.c. phases; i.e., the Ag and Cu are not completely miscible in the solid state. It has been shown that a complete series of solid solutions can be formed by splat cooling of alloys across the entire phase diagram and reliable data exists for the change of lattice parameter as a function of composition. Additionally, the solidus curve for the Cu-rich phase is nearly vertical at the eutectic temperature and this solidus along with the Ag-phase solidus most likely are retrograde when metastably extended below the eutectic temperature. Figure 1 on page 23 shows a phase diagram for Ag-Cu extrapolated into metastable regions using free energy-composition curves which are fit to the regions of stable equilibrium. The existence of these retrogrades are important for they show that in this system enhanced solubility is caused by a trapping mechanism. In this research we will attempt to quantify the solidification conditions under which solute trapping occurs.

9

In an initial set of experiments alloys of eutectic composition (Ag-40 at.% Cu) have been rapidly solidified using the "strip" mode of electron beam surface melting described in the manuscript written for the Lasers in Metallurgy Conference, which is attached to this report, on pages 29 to 38. At relatively slow solidification velocities the microstructures consist of a two phase lamellar eutectic structure with the compositions of the Ag-rich and Cu-rich phases very close to the solubility limits for the phases ($\sim$ 15 at.% Cu and 95 at.% Cu). As the solidification velocities increased, the compositions of these phases should begin to move towards the eutectic composition. At the highest velocities a single phase f.c.c. structure should result with the composition of the eutectic. This final state at high velocity is exactly that observed by Linde and Duwez. We seek to determine the velocity dependence of the solid phase compositions. Strips 3 mm wide were electron beam melted with sample translation rates of 3, 4, 6 and 8 cm/s at constant beam power, producing samples with maximum melt depths ranging between 150 and 10 μm, respectively. Detailed analyses of the solidification velocities present under such conditions can be done to yield calculated velocities. However, the presence of 60 Hz fluctuations in the electron beam deflection system casts some doubt on the present reliability of the processing parameters and, hence, calculations were not performed. These problems are presently being addressed.

The various samples produced were examined with x-ray diffraction and optical and electron microscopy. Surface layers of all of the samples consisted of two phases. Only for the sample surface melted at the fastest speed, 8 cm/s, with a 10 μm melt depth was any change in composition of the two phases noted. X-ray lattice parameter measurements for these phases are shown in Figure 2 on page 24. These data can be converted to composition using the data of Linde and Duwez. The composition of the two phases are

approximately 20 at.% Cu and 42 at.% Cu. Both of these phases are well within
the two phase range for alloys at equilibrium. A micrograph of the surface
melted layer is shown in Figure 3 on page 25. The alloy has lost the lamellar
structure typical of Ag-Cu eutectic alloys and consists of grains of the
supersaturated Cu-rich phase with the supersaturated Ag-phase along the grain
boundaries. Although solute trapping has occurred by E-beam surface melting
in this one case, complete trapping to a single phase material of eutectic
composition will apparently require even higher solidification velocities.

Further experiments are planned in this area which will include alloys of
Ag containing between 10 and 40 at.% Cu. Alloys will be electron beam surface
melted to different depths to obtain various solidification velocities. TEM,
STEM and x-ray analysis of the structures will seek to document the solidification
conditions for the onset of extended solubility, solute trapping, and inverse
dendritic coring.

Calculation of Alloy Segregation Resulting from
Rapid Solidification

One of the long-term goals of this research is to theoretically predict
the amount of microsegregation in rapidly solidified alloys as a function of
the processing conditions. For constant velocity solidification, morphological
stability theory has been used to determine the conditions under which a
planar solid-liquid interface is stable to small perturbations and microsegregation
does not occur. Evaluation of the morphological stability predictions for a
given alloy requires knowledge of a number of thermophysical properties, e.g.
liquid diffusion coefficients and solid-liquid surface free energy. If local
equilibrium prevails at the solid-liquid interface, reasonable estimates of
these properties can be made and the conditions for production of homogeneous

alloys estimated. With increasing solidification velocity, increasing deviations from local equilibrium at the solid-liquid interface are expected. While morphological stability theory has been extended to account for deviations from local equilibrium, the resulting expressions contain a number of quantities, e.g., the dependence of solute distribution coefficient on solidification velocity, which have not been measured. Hence, additional theoretical and experimental research is needed in order to characterize the extent of deviations from local equilibrium during rapid solidification. For example, at high velocities the diffusion boundary layer in front of the solid-liquid interface becomes of atomic dimensions, and the macroscopic diffusion equation should be modified to account for the extremely large solute gradients.

Directional solidification of a binary alloy at constant velocity with an initially planar solid-liquid interface is most amenable to theoretical analysis. Most rapid solidification processes violate one or more of these idealizations. In particular, the treatment of rapid variable velocity solidification would be more directly applicable to a number of experimental techniques of producing rapidly solidified materials.

Except for extremely high velocities, it is to be expected that a number of alloys will exhibit microsegregation. Another effort of this research is to develop a quantitative theory of microsegregation, i.e. alloy composition as a function of position on a microscopic scale. The formulation of the relevant differential equations for the temperature and solute fields and the boundary conditions at the solid-liquid interface is straightforward. However, the numerical solution of the resultant free boundary problem and calculation of solute segregation is not feasible at present despite considerable progress that is being made by a number of research groups using finite element techniques.

Our present effort has involved a number of simplifying assumptions in order to obtain more tractable problems. For example, the lateral solute segregation that results from a curved solid-liquid interface during steady state directional solidification of a dilute binary alloy has been calculated. For a given interface shape, the solute segregation depends on the distribution coefficient k and on the dimensionless parameter (VL/D), where V is the solidification velocity, L the cell size, and D the solute diffusion coefficient in the liquid. The details of the calculation are given in an article to be published in the Journal of Crystal Growth (see pages 39-63). For both very large and very small values of (VL/D) the segregation is small while for intermediate values of (VL/D), dependent on k, the segregation is maximum. The theory permits calculation of solute segregation from an observed interface shape; with additional modification of the numerical algorithm, interface shape could be obtained from an observed segregation profile. However, cell size and interface shape are actually functions of interface velocity and the functional relationships require solution of the general cellular growth problem. Rather than attempt this at the present time, we are extending a simplified model of cellular growth due to Flemings. In this model, (1) the temperature gradient is assumed constant, (2) lateral solute gradients in the liquid are assumed to vanish, and (3) the solid-liquid surface energy is neglected. A prediction of interface shape and solute segregation is obtained, which in the limit of vanishing temperature gradient reduces to the Scheil equation. While this model has certain defects, e.g., for a non-planar interface it predicts an infinite concentration in the cell wall or alternatively that a small amount of second phase will always form, it has been advantageously used in a number of cases at conventional solidification velocities. If we do not make

13

the third assumption, i.e., we retain surface energy terms, a fourth order ordinary differential equation is obtained for the interface shape and solute concentration. The equation is highly non-linear and even its numerical solution has proved difficult. We are presently attempting to develop numerical algorithms to solve this boundary value problem.

In order to properly interpret the rapid solidification experiments described elsewhere in this report, it is necessary to develop numerical methods to calculate solidification velocities since they are not directly measurable. Since such calculations involve a free boundary, viz., the solid-liquid interface, whose position is part of the calculation, they require sophisticated numerical techniques. In addition, the number of processing variables and materials properties are sufficiently large that even when results for a given geometry are available in the literature they are usually not for exactly the parameter range used in an actual experiment in our laboratory. Basically, the numerical program should be executed for precisely those parameters used in an actual experiment. For this reason, we have spent considerable effort to develop numerical algorithms to calculate solidification velocities for particular experimental geometries; this work has been in collaboration with Drs. Charles Fenimore and R. F. Boisvert of the NBS Center for Applied Mathematics. Previously we developed an algorithm for solving the one-dimensional time-dependent heat flow equation (with phase change) applicable to electron beam or laser melting. At present, we are developing an algorithm for the two-dimensional steady-state heat flow equation (with phase change) applicable to the moving line source method of electron beam or laser melting.

14

Rapid Solidification Microstructures in Al-Ag Alloys

from Electron Beam Melting Studies

Electron beams have been used to carry out surface melting of several different alloys, with an emphasis on detailed characterization of the thermal input. The major objective is to relate microstructures to the thermal conditions which prevail during solidification, and these conditions can be calculated only if the distribution of the electron beam energy in space and time are sufficiently well known. Procedures have therefore been developed to measure the energy distributions in electron beams and to scan the beam electronically to produce surface melting which is effectively uniform in either one or two dimensions. These procedures are described in the attached report on pages 29 to 38, "Controlled Rapid Solidification by Electron Beam Heating" by R. J. Schaefer, W. J. Boettinger, F. S. Biancaniello and S. R. Coriell, which has been submitted for publication in the proceedings of the "Lasers in Metallurgy" sessions which were held at the February 1981 meeting of The Metallurgical Society of AIME in Chicago.

Al-Ag alloys with 0.1 to 1.0 wt. percent silver have been surface melted to produce growth velocities which are predicted to be on both sides of the boundary between the regimes of instability and absolute stability. All of these samples have shown cellular microstructures, which are sometimes very regular and periodic and at other times show no regular periodicity. These observations are also described in the attached report.

Plans for the immediate future include detailed studies of the Al-Ag system using several of the melting modes available with the electron beam, and correlation of the observed microstructures to the growth velocities and temperature gradients. Of particular importance is the question of the behavior of a cellular interface which undergoes an acceleration of growth

velocity which moves it into the regime of absolute stability. If such an interface does not rapidly revert to plane-front solidification, then the accurate measurement of absolute stability effects in surface melted materials will require analysis of the entire cycles of growth velocity, temperature gradient and concentration gradient which occur during solidification, instead of just the instantaneous values at the point where the microstructure is observed. In all of the different modes of surface melting, the solid-liquid interface starts with zero growth velocity and accelerates to its maximum value, but by changing the melting parameters, one can vary the trajectory of an interface on a temperature gradient vs. growth velocity plot and may be able to attain conditions under which the region of morphological instability is completely avoided. In all cases, caution must be exercised in the application of morphological stability theory when the solidification parameters are time-dependent.

Microstructural study of Al-Ag surface melts has revealed some influence of crystal anisotropy and tests will be carried out to determine if this factor influences the planar to cellular transition, or if it merely changes the orientation of the microstructure.

Long-range plans call for study of residual stress effects in surface melted samples. The importance of these effects is dramatically evident in many surface melted materials in the form of cracking which frequently extends throughout the melt zone and often into the unmelted substrate. In addition, severe warping may occur even when the sample thickness is many times the depth of the melt zone. Both of these effects indicate that the surface layer formed by rapid solidification is in a state of high tensile stress, which is a generally undesirable situation.

Many of the cracks in surface melted samples appear to be the result of hot tearing - the pulling apart of the material at grain boundaries or between

16

dendrites during the solidification process. To make useful surface coatings, this type of cracking must be eliminated since it cannot be rectified by post-melt processing. The prevalence of the effect varies strongly with alloy composition, and some quantitative data on the occurrence of cracks as a function of this variable should be obtained. However, in practical situations one is not free to make large changes in alloy composition and a potentially more useful approach to controlling cracking would be through variations of the surface heating mode or thermal cycle.

In systems where cracking has not occurred during the surface melting process, it may still be desirable to relieve the surface stresses. Although it is clear that this can be done by annealing treatments, it is not clear that it can be done without the loss of some of the desirable properties which motivated the surface melting process. Therefore, it will be of interest to study various annealing strategies including brief transient anneals with directed-energy sources at powers less than that required for surface melting.

Metallic Glass Formation

(a) Introduction

Research continued on the relationship between eutectic solidification and the formation of metallic glass. The theory of how rapidly one needs to solidify to obtain a glassy structure has usually focussed on the nucleation of the solid phase as the difficult step in crystallization. In the present work, the focus instead has been on the growth process. Diffusional sorting of alloy components is necessary to form a two-phase eutectic composite structure. Theoretical predictions made of the limitation this imposes on the growth rate, predict that at sufficiently rapid solidification rates this diffusional sorting would no longer be possible. In that case one could expect amorphous solids to be formed. Experiments performed during the first year of this contract under conditions where the solidification velocity was increased during the solidification process showed an abrupt change from crystalline to metallic glass microstructure in Pd-Cu-Si alloys at a critical velocity. Since the amorphous material was formed while in direct contact with the crystalline material, nucleation would not be a limiting factor here. Thus, the observed transition from crystal to metallic glass caused by accelerating the solidification rate indicates the importance of growth rate in producing these amorphous microstructures.

Work during the current reporting period was focussed in the following areas involving Pd-Cu-Si alloys.

1. The effect of composition on the critical velocity for glass formation has been investigated. It is well known that alloys containing ∿ 6 at.% Cu ∿ 17 at.% Si form glass most easily.

18

Increasing or decreasing the copper content decreases the ease of glass formation. We have investigated the effect of varying copper content on the microstructure of the alloy at different solidification velocities and the transition to the glass.

2. Compositional analysis of phases present in the above alloys has been performed. Because the ternary phase diagram for Pd-Cu-Si alloys is poorly known such information is necessary to permit an assessment of the thermodynamic limitions which are present during rapid quenching of these alloys.

(b) Alloys and Phase Determination

Alloys have been prepared from 99.99% pure components of the following compositions lying roughly on a line in the ternary system.

Number	at.% Pd	at.% Cu	at.% Si
8000	78	1.4	20.6
11000	78	4	18
7000	77	6	17
10000	76	9	15
9000	73	12	13.5

Cooling curves have been conducted on these alloys. In addition to primary crystallization at various temperatures, all three alloys complete solidification with a eutectic arrest at 734 ± 2 °C. This indicates that all three of these alloys most likely complete solidification with a eutectic involving the same phases. Microstructural and microprobe analysis confirms this fact and shows the eutectic to consist of Pd_9Si_2 and a phase denoted κ

having a variable composition between $Pd_{73}Cu_{15}Si_{12}$ and $Pd_{55}Cu_{36}Si_8$. The phases Pd_3Si and Pd_9Si_2 also occur as dendritic phases in the 1.4, 4 and 6 at.% Cu alloys.

To assess the effect of solidification velocity on these alloys, thin alloy-filled quartz tubes (0.75 mm ID x 1.5 mm OD x 10 cm long) are quenched in the axial direction from a furnace at 1100 °C into liquid Ga at various speeds. Samples are quenched in two stages: the first at a relatively slow speed (0.25 mm/s) to establish a crystalline substrate; and the second at various speeds up to 10 mm/s. This procedure eliminates bulk undercooling of the entire sample and permits the study of growth kinetics under known conditions.

At an interface velocity of 0.25 mm/s, the 4 and 6 at.% Cu alloys have the following solidification path. Dendrites of Pd_3Si form at the highest temperature followed by faceted dendrites of Pd_9Si_2. The monovariant peritectic $L + Pd_3Si \rightarrow Pd_9Si_2$ is completely suppressed. Since both of these solid phases contain very little Cu (< 1 at.%), the interdendritic liquid is enriched in Cu until the monovariant eutectic trough $L \rightarrow Pd_9Si_2 + \kappa$ is encountered. This reaction completes solidification with no sign of the ternary eutectic $L \leftrightarrow Pd_9Si_2 + \kappa + \alpha\text{-Pd}$ (same structure as Fig. 4a shown on page 26). This indicates that the slope of the monovariant eutectic trough is very small. These observations are consistent with the topology of the Pd-Cu-Si liquidus surface proposed by Massalski et al. (ref. 3). However, compositions of the various monovariant lines may differ slightly. The 9 at.% Cu alloy consists only of eutectic at a solidification velocity of 0.25 mm/s.

(c) Rapid Quenching - 4 and 6 at.% Cu Alloys

As the velocity is increased the dendritic phase of Pd_9Si_2 disappears while the dendrites of Pd_3Si remain. Consequently, the volume fraction of eutectic increases. This occurs at 5 mm/s for the 4 at.% Cu alloy and $\sim$ 0.5 mm/s for the 6 at.% Cu alloy (Fig. 4). At a velocity of 1 mm/s the Pd_3Si dendrites disappear from the structure of the 6 at.% Cu alloy. Interestingly this disappearance of the Pd_3Si dendritic phase from the microstructure does not occur for the 4 at.% Cu alloys until the solidification velocity exceeds 5 mm/s. This large difference between the speeds required to convert the structures from dendritic to eutectic for the 4 and 6 at.% Cu alloys (1 mm/s vs. 5 mm/s) is correlated with the large difference in the critical velocities required to form glass in these alloys (2.5 mm/s vs. 10 mm/s). An interesting point to note in 4 at.% Cu alloys solidified at speeds in excess of 2.5 mm/s, is that the eutectic grains are not continuous in the growth direction. They appear to grow laterally from the pre-existing dendritic structure (Fig. 5). This observation is consistent with the fact that the eutectic structure itself cannot grow at speeds much greater than 2.5 mm/s. By growing laterally, such eutectic grains can complete solidification at slower rates. The important feature here is that until the dendritic solidification ceases, the alloy cannot be made amorphous. The conversion of the microstructure to fine eutectic appears to be a necessary precursor of glass formation. Continued increases in solidification velocity beyond this stage leads to a sharp interface, reported previously, between the eutectic microstructure and amorphous alloy (Fig. 6).

21

(d) Rapid Quenching - 9 at.% Cu Alloy

The 9 at.% Cu alloy behaves quite differently. The alloy is essentially devoid of dendritic phases at all solidification velocities. The eutectic-like microstructure becomes more refined with increasing solidification velocity until at $\sim$ 2.5 mm/s, the structure converts to a mixture of glassy alloy and 25 μm diameter crystallites (Fig. 7). Presumably the liquid in front of the freezing liquid (which must be highly undercooled) reached the nucleation temperature of some phase. The identity of the phase or phases of which these crystallites are composed is currently under investigation. Quenching at higher rates up to 1 cm/s still leads to a mixture of crystallites and glass. Hence, the reasons for the increased difficult of making a completely glassy alloy for the composition is related to the formation of these crystallites.

References

1. J. Murray, to be published.

2. R. K. Linde, J. Appl. Phys. 31 (1960) 1136.

3. T. B. Massalski, Y. Kim, L. F. Vassamillet and R. N. Hopper, Mat. Sci. and Eng. 47 (1981).

THE SYSTEM SILVER–COPPER
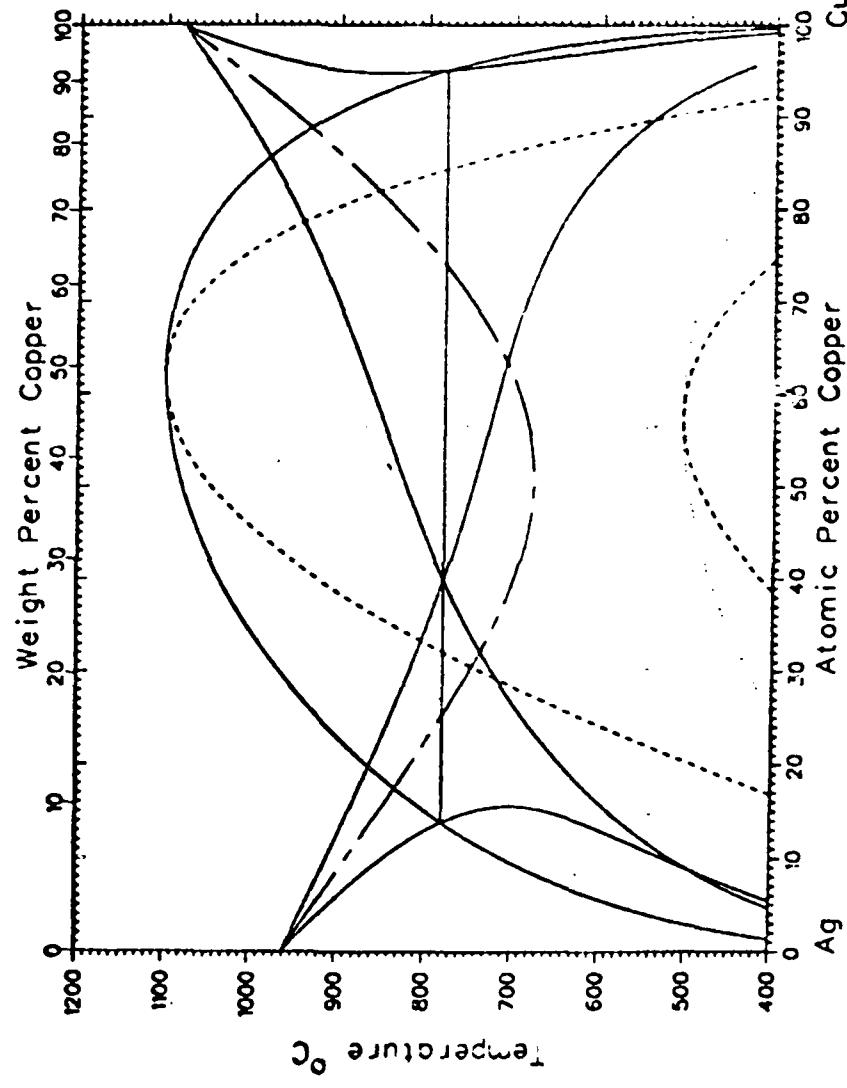
Fig. 1. Ag-Cu diagram including metastable extenstions of two phase equilibrium, solid lines; spinodal curves, dashed lines; T_0 curve for partitionless solidification, short-long dashed lines; and metastable liquid miscibility gap, dotted (ref. 1).
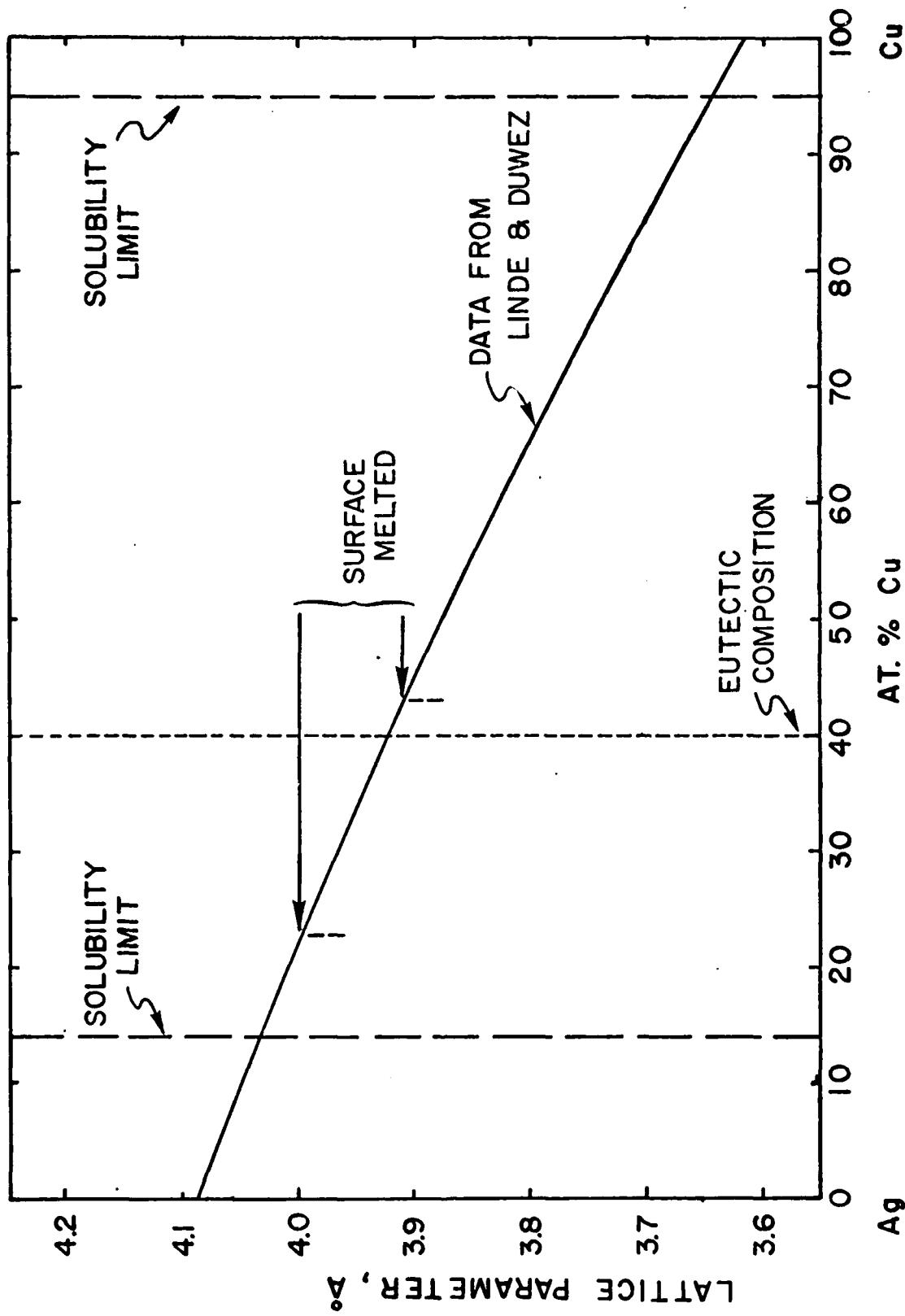
Fig. 2. Lattice parameter vs. composition for FCC Ag-Cu alloys; solid line (ref. 2). Measured lattice parameters of two phases present in electron beam surface melted Ag-Cu eutectic.
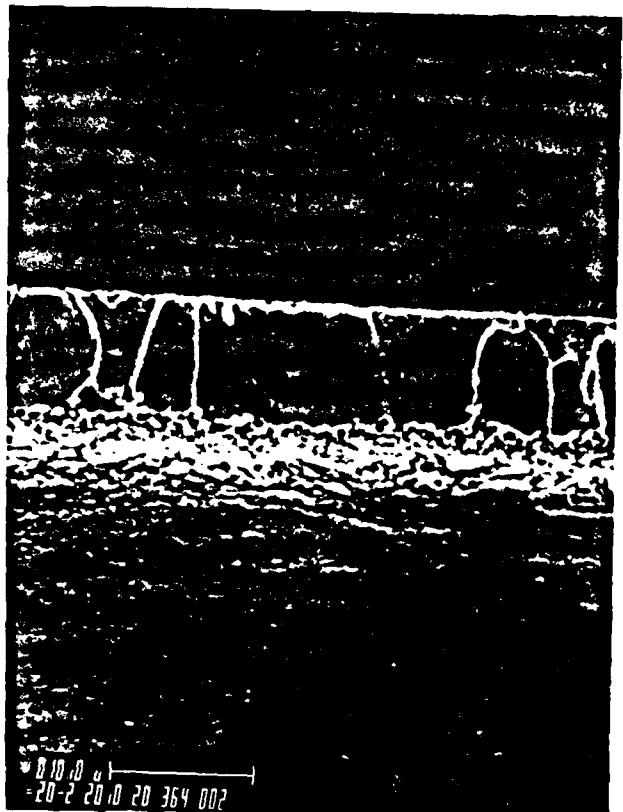
Fig. 3.   SEM view of transverse section of
surface melted layer of Ag-Cu eutectic
alloy.   The mark is 10 μm in length.
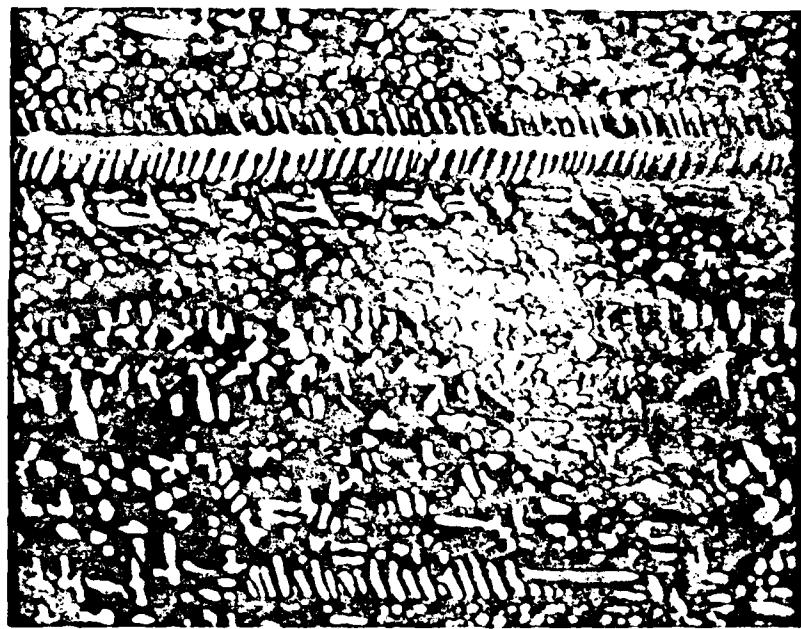
(b)
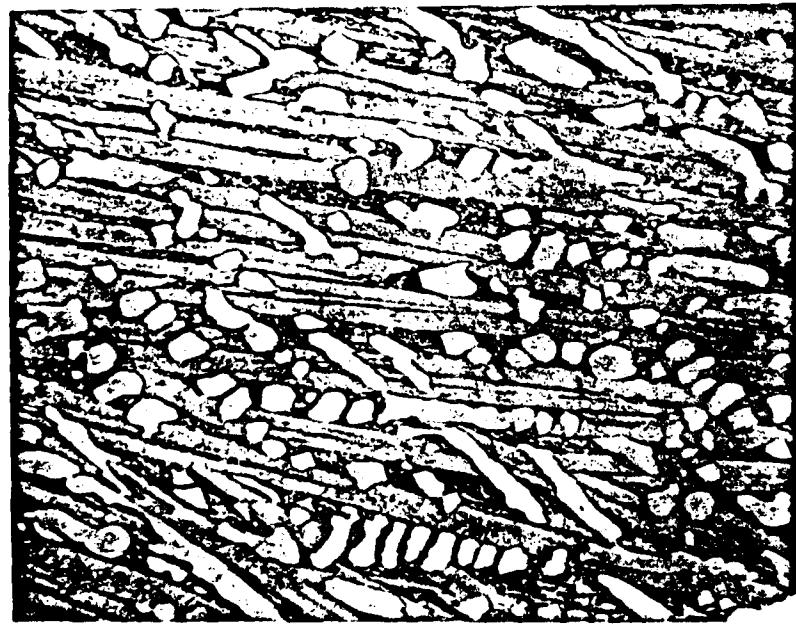
(a)

Fig. 4. Optical micrograph of Pd-4 at.% Cu-18 at.% Si alloy directionally quenched with solidification velocities of a) 1 mm/s and b) 5 mm/s. Note the disappearance of the facetted phase in b. 800X.

26

Fig. 5. Optical micrograph of Pd-4 at.% Cu-18 at.% Si
alloy solidified at 5 mm/s showing presence of
many eutectic grains. 80X.
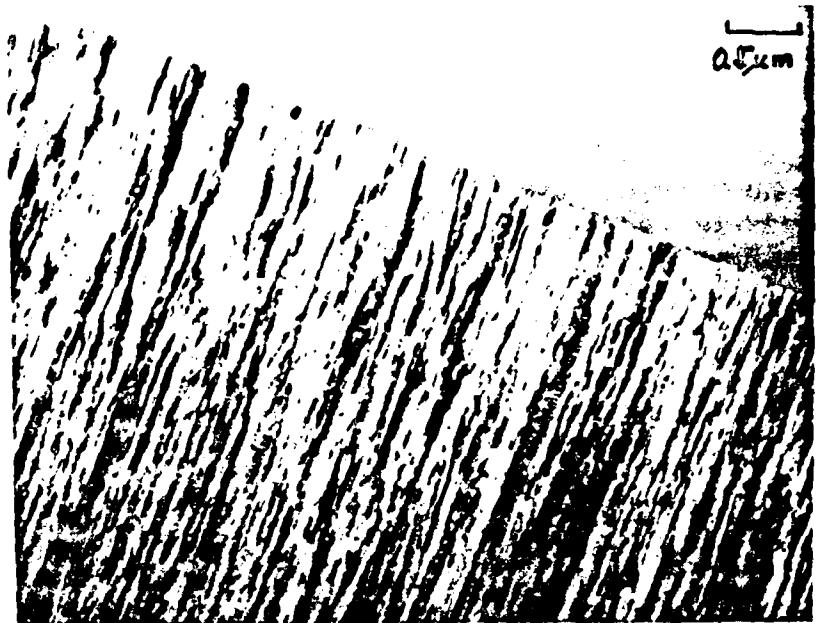
Fig. 6. TEM micrograph of the interface between fine multiphase crystalline alloy and glassy alloy. This interface is obtained during directional quenching experiments and represents the position in the sample where the maximum eutectic crystallization velocity is achieved.

Fig. 7. Optical micrograph of interface between fine eutectic structure and glass + crystallite region formed when a Pd-9 at.% Cu-15 at.% Si alloy is quenched at 2.5 mm/s. 80X.

CONTROLLED RAPID SOLIDIFICATION BY ELECTRON BEAM SURFACE MELTING

R. J. Schaefer, W. J. Boettinger, F. S. Biancaniello, and S. R. Coriell
National Bureau of Standards
Washington, D.C.

The use of a modified electron beam welding apparatus to produce controlled rapid solidification is described. For research purposes, electron beam heating has several advantages over laser heating, most significantly that the absorbed power is known better and the beam can be deflected electronically at high speed. Experiments can thus be carried out in which local solidification velocities can be determined from the known thermal input by means of heat flow calculations. We report here several methods of utilizing electron beam heating, and some observations of cellular substructures in surface melted Al-Ag alloys.

The melting of thin layers on metal surfaces by directed energy sources such as lasers or electron beams can result in rapid resolidification as heat is conducted into the cooler substrate. Such surface layers can have any of the structural characteristics which have been observed in rapidly solidified metals, such as amorphous or highly supersaturated crystalline phases, or highly refined microstructures. For studies attempting to correlate these structures to the thermal conditions prevailing during solidification, surface melting has an advantage over other rapid solidification processes such as spray atomization or melt spinning in that no coefficient for the transfer of heat from the metal to an external cooling medium need be estimated. Calculations of the melting and freezing of metals subjected to surface heating by directed energy sources (1-4) can thus be used with relative confidence, provided that the thermal input of the energy source can be adequately characterized.

The objective of the research reported here has been to relate the microstructure of surface melted layers to the solidification conditions, and to use the observed relations to test and improve upon theories of rapid solidification (5, 6). Experimental data of this type are needed to better define, for example, the possible dependence of solute distribution coefficients on solidification velocity.

For the purpose of producing well-characterized thermal inputs for these experiments, electron beam heating has certain advantages, to be discussed below. We seek especially modes of heating which will produce solidification conditions which are homogeneous over sufficiently large areas that the microstructural analysis does not depend on a knowledge of the exact location of the sample within the melt.

Energy Input to Metal Surfaces

Although lasers have several attractive characteristics as instruments for surface heating, it is difficult to predict how much of the energy in an incident laser beam will be absorbed by a metal surface, especially at high power densities. The variation of absorptivity with temperature and wavelength can be reasonably well accounted for, but the dependence of the energy absorption on sample surface condition is a rather unpredictable factor which may change greatly when the surface oxidizes or a surface layer becomes molten. Therefore the melting and freezing of the surface can be more reliably calculated if the thermal energy input is provided by an electron beam.

When a beam of high-energy (10-100 keV) electrons impinges upon a metal surface, a fraction of the electrons are elastically backscattered with little transfer of energy to the metal. The backscattered energy increases with larger atomic number targets, so that for 30 keV electrons one would expect elastic backscattering to produce a 7% energy loss for an aluminum target but almost a 35% loss for a uranium target (7). Although x-rays are generated at intensities which demand safety measures such as the use of leaded glass in viewing ports, the energy loss in this form is minute.

The electron beam current actually entering the target can readily be monitored by observing the voltage across a resistor by which the target is connected to ground. By means of such a device, one can observe that as the beam power density is increased the current entering the sample suddenly

falls sharply (about 20-30 percent in a typical case) when a plasma is ignited above the target surface. This is clearly a situation to be avoided in quantitative melting experiments, for in the presence of the plasma one does not know how much energy remains in those electrons which do reach the target surface, or how much of the energy which is given up to the plasma is subsequently transferred to the target by secondary processes. McKay and Schriempf (8) have carried out a calculation of the energy transferred to a metal surface by the thermal emission (mostly ultraviolet) from a laser-induced plasma above the metal surface, but it has yet to be shown that such a calculation can attain high accuracy.

Equally as important as a knowledge of the total energy entering the target is a knowledge of the spatial distribution of the energy. We have used several devices for measuring beam profiles, based on modifications of devices reported in the literature (9). With either lasers or electron beams, it is usually easier to measure the beam profile at much lower beam powers than those used for the actual surface melting, or at some plane other than the target plane, where the beam is expanded to a much lower power density. We have sought methods which allow beam profile measurements in the target plane at fairly high beam currents.

An easily constructed profile-measuring device for use with electron beams consists of an array of parallel fine tungsten wires (Fig. 1a). The electron beam is scanned rapidly across the array and the current entering the wires is recorded on an oscilloscope. If the wire diameter is small compared to the beam diameter, the peaks seen on the oscilloscope show the beam profile. The multiple wires facilitate the determination of the beam scanning velocity. This device can be used only at relatively low power levels if the wires are to survive.

Another device, which is shown in Fig. 1b, is similar in concept to that shown in Fig. 1a, but in this case the signal on the oscilloscope represents the current which passes through the narrow slit between the two knife edges as the electron beam is scanned across it. The advantage is that the knife edges, especially if they are water cooled, can tolerate a considerably higher beam current than could the fine wires. In the device as shown, the beam current passing through the slit is captured by a Faraday cup, which collects most of the backscattered electrons as well as those that are directly absorbed by the bottom of the cup. The device could readily be modified to count only the directly absorbed electrons, but this would change only the amplitude, and not the shape, of the re-corded signal.
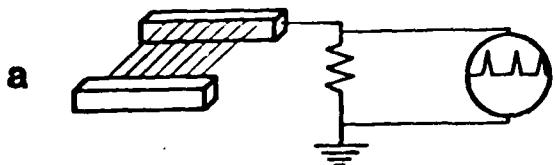

Fig. 1. Devices for measuring electron beam current dis-tributions. (a) Multiple wire device (b) Slit and Faraday cup device.
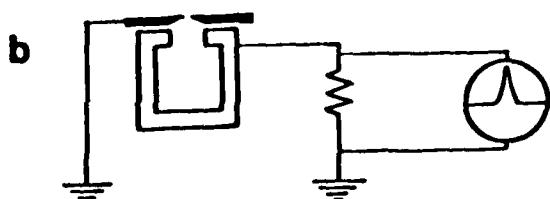
Both the wire and the slit device measure the current in a narrow strip passing through the electron beam. Except for a simple gaussian-shaped beam, it is difficult to deconvolute this information into an exact description of the current as a function of position, and impossible if the beam is not radially symmetric. This information can be obtained by replacing the slit of Fig. 1b by a pinhole and scanning the beam over the pinhole repetitively in one direction while scanning at a slower rate in the perpendicular direction. One thereby obtains a useful oscilloscope trace which represents a series of cross-sectional slices through the beam profile.

Our measurements of beam profiles, using the devices shown in Fig. 1, have shown that the most sharply focused beam is approximately gaussian in profile with a FWHM of approximately 10^{-4}m. At focusing current greater than that required for sharp focus, the beam becomes wider but with a sharp central peak, whereas at lower focusing current the beam becomes wider with a flat top or with a higher power around the perimeter.

Useful Heating Modes

Fig. 2 illustrates schematically some of the modes of surface heating which are being used to produce rapidly solidified metals. The line and strip are steady state modes in a moving reference frame, whereas the spot, patch and pedestal are transient or pulsed modes.

A full heat-flow analysis of the spot mode has been published (2), but this is a situation in which the solidification parameters vary from point to point with only radial symmetry. It is thus not ideally suited for microstructural studies.

In the line mode, a beam sweeps at constant velocity across the target surface, leaving behind a linear trail. This mode, which has also been analyzed (3), has the advantage over the spot mode that any cross-sectional cut perpendicular to the direction of motion should show an identical configuration.
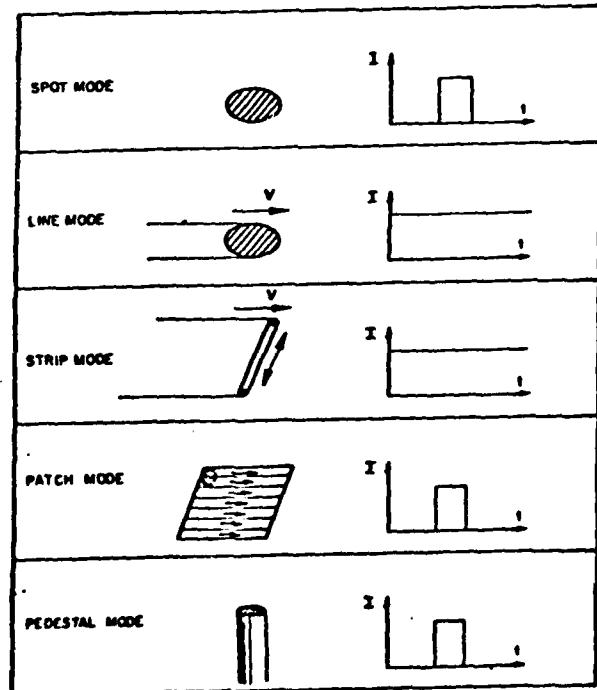

Fig. 2. Modes of surface melting which can be carried out with an electron beam, showing for each the time dependence of the beam current.

The strip mode uses a beam which is electronically scanned very rapidly back and forth to simulate a line source of heat with a width which is equal to the beam diameter and a length which is determined by the electronic deflection. The simulation is effective only if the scanning is sufficiently rapid that the heating appears continuous at a small distance below the surface. The target is translated perpendicular to the direction of the electronic scan, leaving behind a wide, shallow melt pass. In this mode, freezing conditions can be uniform across the width of the strip except near the edges, so that large areas of sample with identical processing conditions can be obtained. However, the heat flow analysis of this mode has not yet been carried out.

The patch mode is a method for producing uniform heating over an extended area. Ideally one could simply use a large diameter beam with uniform intensity, but this is in practice not readily attained. It is therefore simulated by rapidly rastering a beam over a patch so that the average power density has the desired value. Once again, the rastering must be sufficiently rapid to appear continuous at the maximum melt depth. The objective of this mode is to produce uniform heating over an area sufficiently large that the heat flow is effectively one-dimensional and the solidification conditions depend only on the depth below the surface. In the pedestal mode the patch covers the entire end of a rod-shaped sample, so that heat flow is approximately one-dimensional even if the pulse time is rather long.

Fig. 3 illustrates the range of power density and pulse time combinations which can be used with the patch mode for surface melting of aluminum. The lower boundary of the trapezoid represents the critical value of $q\tau^{\frac{1}{2}}$ required to get the surface just barely to the melting point (1), where q is the beam power density and τ is the pulse duration. The upper boundary is the value of $q\tau^{\frac{1}{2}}$ at which the average metal surface temperature reaches the boiling point (at atmospheric pressure). The left side of the trapezoid represents the minimum time required to complete 10 scans of the patch (at 4 kHz) while the right side limit represents the maximum pulse time for which the machine has sufficient power (10 kW in our case) to melt an area sufficiently large to attain one-dimensional heat flow. Because electron beam melting is carried out in a vacuum, it is not reasonable to expect the surface of the metal to reach the atmospheric pressure boiling point (at least not without violent side effects), so operations should be confined to the lower part of the trapezoid. In addition, the smaller the beam size in relation to the patch size and the smaller the total number of raster scans during the pulse time, the
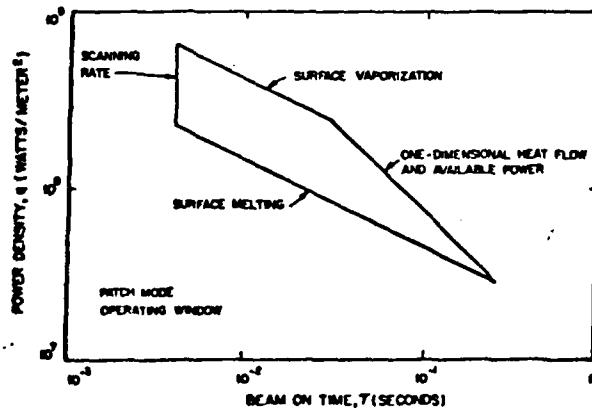

Fig. 3. Operating window for surface melting of aluminum in the patch mode.

33

hotter is the local transient surface temperature directly under the beam. To avoid the danger of local overheating, it is best to defocus the beam so that its diameter is perhaps one half the width of the patch and to scan as rapidly as possible.

Alloy Solidification

One of the most important characteristics sought in rapidly solidified metals is chemical homogeneity. Previously published calculations (5, 6) have indicated that at sufficiently rapid rates of solidification, metals can solidify with stable solid-liquid interfaces at alloy concentrations much greater than those predicted for instability by constitutional super-cooling theory. This regime of "absolute stability" can be attributed to the influence of the solid-liquid surface energy in opposing the growth of perturbations with very short wavelengths.

The previous calculations for Al-Cu and Si alloys, which assumed that the solute distribution coefficient was that given by the equilibrium phase diagram, indicated that the transitions from instability to absolute stability should occur at very low alloy concentrations or at very high interface velocities. We have chosen to work with the system Al-Ag because it has a rather high solute distribution coefficient (k = 0.41) which results in a predicted range of interesting stability-instability transitions at compositions of 0.1-1 wt.%.

In Fig. 4 the curved line shows the behavior of this alloy system as predicted by morphological stability theory, while the straight lines indicate the predictions of simple constitutional supercooling and absolute stability criteria (5, 6). The physical properties used in the calculations are listed in Table I.
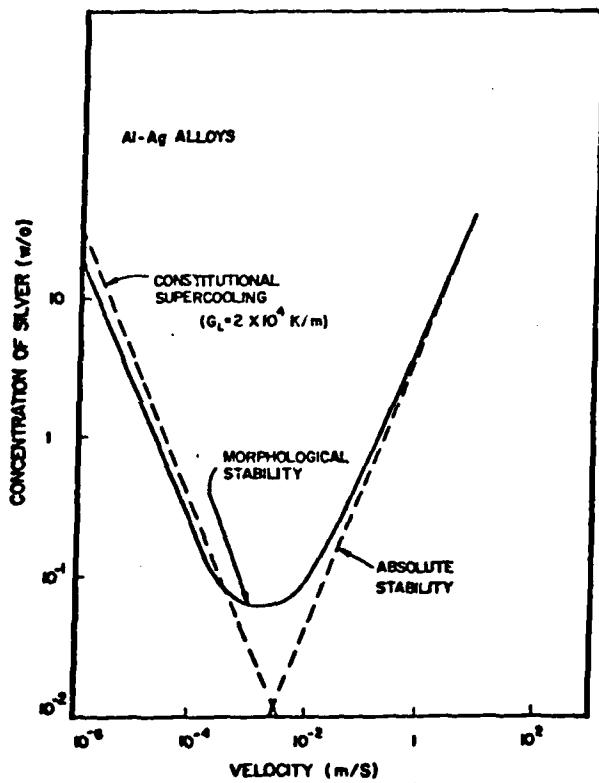

Fig. 4. Stability of planar interfaces in Al-Ag alloys.

34

Table I. Properties Used for Stability Calculation. in Al-Ag

Property	Symbol	Value
Diffusion coefficient in liquid	D	$4.5 \times 10^{-9} \, m^2 s$
Solute distribution coefficient	k_o	0.41
Liquidus slope	m	-1.7 K/wt.%
Surface energy parameter	$T_M \Gamma$	$1.0 \times 10^{-7} \, mK$
Latent heat of fusion	L	$1.08 \, GJ/m^3$
Thermal conductivity of liquid	k_L	90.4 J/msK
Thermal conductivity of solid	k_S	211 J/msK
Thermal diffusivity of liquid	κ_L	$3.5 \times 10^{-5} \, m^2/s$
Thermal diffusivity of solid	κ_S	$6.8 \times 10^{-5} \, m^2/s$

The constitutional supercooling line is given by

$$c_\infty = \frac{G_L D k}{v(k-1)m}$$

where G_L is the temperature gradient in the liquid, D is the interdiffusion rate in the liquid, k is the solute distribution coefficient, v is the velocity of solidification, and m is the slope of the liquidus curve.

The absolute stability criterion predicts

$$c_\infty = \frac{k^2 T_m \Gamma v}{D(k-1)m}$$

where T_m is the melting temperature and Γ is the ratio of the solid-liquid surface energy to the latent heat of fusion per unit volume.

The calculation was carried out assuming that the solute distribution coefficient does not depend on velocity. If there is a dependence, one would expect the distribution coefficient to approach unity at higher velocities, which would lead to additional stabilization of planar inter-faces. The concentrations for instability on the left side of the curve are approximately proportional to the temperature gradient in the liquid (here assumed to be 200 K/cm), but the concentrations on the right side are almost independent of gradient.

There exists a body of experimental experience which demonstrates the type of behavior described by the left side of Fig. 4 but the absolute stability transition on the right side has never been accurately measured, although evidence for this transition has been reported for laser-melted Si (10, 11). Conventional solidification processes cannot attain the required velocities, and in most rapid solidification processes the interface

35

velocity is not well enough known for a meaningful correlation to the theory. Well-controlled surface melting can be used to investigate this region.

Our experiments with Al-Ag alloys have used samples with 0.1, 0.3, and 1.0 wt.% silver. Line mode tracks have been melted using an electron beam 1 mm in diameter sweeping over the sample surface at velocities of 0.05, 0.15, and 0.42 m/s. At these velocities, plane-front solidification is predicted to be unstable at silver compositions above 0.28, 0.71, and 1.8 wt.% Ag, respectively. If the sweep velocities were equal to the actual interface velocity, then most of these samples would have been in the absolute stability regime. However, when the samples were sectioned, and examined by scanning electron microscopy, it was found that cellular structures were present throughout all melt passes, except for a very thin layer near the bottom of each pass which represents an initial transient in the melt pool solidification. The observed structures are sometimes elongated cells but in other regions are rather irregular arrays with occasional very small regions of hexagonal symmetry (Fig. 5).

At steady state in the line mode of melting, local solidification velocities must everywhere be less than the sweep velocity of the beam across the sample surface, by a factor equal to the cosine of the angle θ between the normal to the interface and the direction of the sweep.

Some of the curves shown in Ref. (3) were computed for melting parameters close to those used in these experiments, so they may be used to estimate local interface velocities. Thus within the central regions of the melt pass, the local solidification velocity should be no less than about 50% of the sweep velocity. This factor is insufficient to move the experimental points into the theoretically unstable region of Fig. 4.
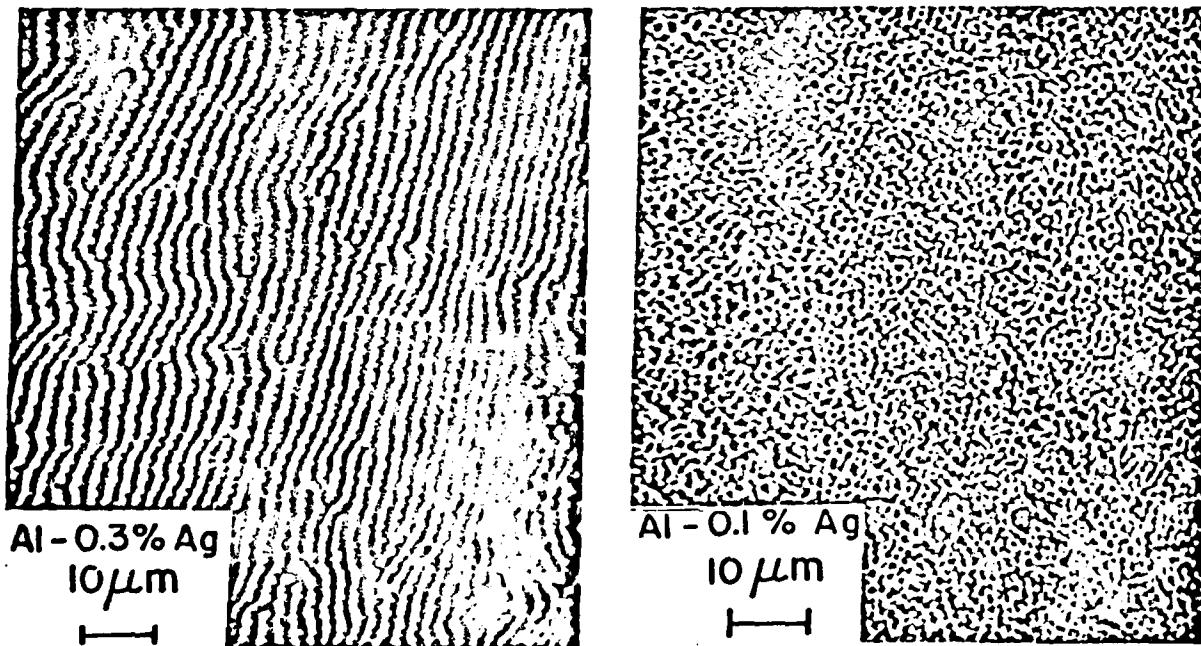

Fig. 5. Examples of well-developed elongated cells and irregular arrays in electron-beam melted Al-Ag alloys. Both samples melted in line mode with sweep speed 0.05 m/s.

36

Other factors which could account for the observation of cells when none were expected include inaccuracy in the parameters used in the theory, especially the diffusion coefficient D, which was obtained from macrosegregation experiments (12), and the surface energy term Γ. In addition, all of the interfaces in this experiment which were predicted to be in the absolute stability regime had propagated through regions near the bottom of the melt which would have been in the unstable regime. Once the cellular structure is developed in this region, we do not know that the conditions required to restore planar solidification are the same as those required for a planar interface to break down, nor do we know how long a transient may be required for the restoration of planar solidification. Thus a cellular interface may continue to propagate in the cellular mode even in regions where a planar interface would be stable. This subject requires further study.

Cell spacings were measured in some of the more regular structures, and they showed good agreement with the predicted wavelength at the onset of instability, when plotted as a function of velocity (Fig. 6). However, some of the measured cellular structures lay well within the predicted region of absolute stability, so the significance of the agreement is unclear.

More experiments with these alloys, using different melting modes, will be required before any firm conclusions can be drawn with respect to the correct location of the absolute stability limit.

Acknowledgments
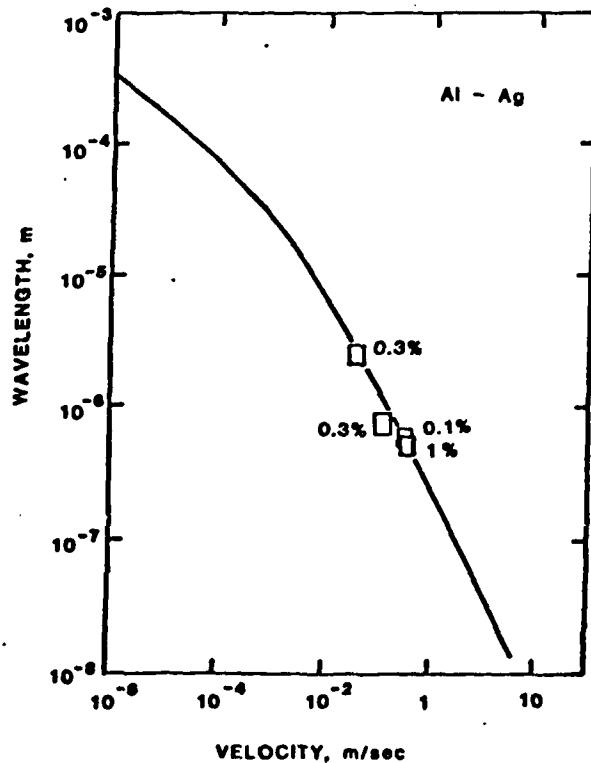
Fig. 6. Wavelength at the onset of instability as a function of solidification velocity. The plotted uncertainty in the experimental points represents a variation between 0.5 and 1 of the cosine of θ, which is the angle describing the local growth direction.

37

References

1. S. C. Hsu, S. Chakravorty, and R. Mehrabian, "Rapid Melting and Solidification of a Surface Layer," Metallurgical Transactions 9B (1978) pp. 221-229.

2. S. C. Hsu, S. Kou and R. Mehrabian, "Rapid Melting and Solidification of a Surface Due to a Stationary Heat Flux," Metallurgical Transactions 11B (1980) pp. 29-38.

3. S. Kou, S. C. Hsu and R. Mehrabian, "Rapid Melting and Solidification of a Surface Due to a Moving Heat Flux," Metallurgical Transactions 12B (1981) pp. 33-46.

4. R. Mehrabian, S. C. Hsu, S. Kou, and A. Munitz, "Laser Surface Melting and Solidification - Moving Heat Flux," pp. 213-227 in Applications of Lasers in Materials Processing, E. A. Metzbower, ed.; ASM, Metals Park, Ohio, 1979.

5. S. R. Coriell and R. F. Sekerka, "Interface Stability During Rapid Solidification," pp. 35-49 in Rapid Solidification Processing: Principles and Technologies, II, ed. R. Mehrabian, B. H. Kear and M. Cohen, Claitor's Publishing Division, Baton Rouge, La., 1980.

6. J. W. Cahn, S. R. Coriell and W. J. Boettinger, "Rapid Solidification," pp. 89-103 in Laser and Electron Beam Processing of Materials, ed. C. W. White and P. S. Peercy, Academic Press, New York, 1980.

7. M. von Allmen, "Coupling of Beam Energy to Solids," pp. 6-19, Ibid.

8. J. A. McKay and J. T. Schriempf, "Transient Heating of Metals by Microsecond-Duration CO_2 Laser Pulses with Air Plasma Ignition," pp. 55-60 in Laser-Solid Interactions and Laser Processing, ed. S. D. Ferris, H. J. Leamy and J. M. Poate, American Institute of Physics, New York, 1979.

9. Y. Arata, E. Nabegata, and N. Jamoto, "Tandem Electron Beam Welding," Transactions of JWRI, 7 (1978 p. 85.

10. J. Narayan, "Interface Instability and Cell Formation in Ion-Implanted and Laser-Annealed Silicon," to be published.

11. A. G. Cullis, D. T. J. Hurle, H. C. Webber, N. G. Chew, J. M. Poate, P. Baeri and G. Foti, "Growth Interface Breakdown During Laser Recrystallization from the Melt," Applied Physics Letters 38 (1981) pp. 642-644.

12. S. Asai and I. Muchi, Tetsu to Hagane, 65 (1979) pp. 203-211 (in Japanese).

Lateral Solute Segregation During Unidirectional Solidification

of a Binary Alloy with a Curved Solid-Liquid Interface II:

Large Departures from Planarity

by

S. R. Coriell, R. F. Boisvert, and R. G. Rehm

National Bureau of Standards

Washington, DC   20234

and

R. F. Sekerka*

Carnegie-Mellon University

Pittsburgh, PA 15213

*   Consultant, National Bureau of Standards

ABSTRACT

The lateral solute segregation that results from a curved solid-liquid interface during steady state unidirectional solidification of a dilute binary alloy is calculated by analytical and numerical methods for large departures of the interface shape from planarity. These calculations are an extension of previous results obtained by perturbation theory for the case where there are small departures of the interface from planarity. Numerical results are given for a sinusoidally shaped interface for various values of the distribution coefficient, k, and the parameter $\beta = VL/D$ where V is the velocity of solidification, L is the wavelength of the sinusoidal perturbation, and D is the diffusivity of solute in the liquid. For both very large and very small values of β, the segregation is small and proportional to the amplitude of the sinusoidally shaped interface. For intermediate values of β, dependent on k, the segregation is maximum and no longer proportional to the interface amplitude; the segregation profiles along the interface are distorted such as to be flat near projections of solid into the liquid and rapidly varying near projections of liquid into the solid.

40

1. INTRODUCTION

In a previous paper [1], we developed an analytical expression for the lateral solute segregation associated with the curvature of a nearly planar solid-liquid interface during steady state unidirectional solidification of a binary alloy. This expression was based on an assumed interface shape and a consistent solution, by linear perturbation methods, of the steady state diffusion equation.

In the present paper, we extend these results by analytical and numerical methods to the case where the solid-liquid interface departs significantly from planarity. As in our previous paper, we treat only a two dimensional problem and do not attempt to reconcile our assumed interface shapes with a self-consistent thermal field.

2. THEORY

We wish to determine the effect of a non-planar solid-liquid interface on the solute distribution during unidirectional solidification of a binary alloy at constant velocity V. We consider a container of width L as shown in Fig. 1 and choose a coordinate system moving with the solid-liquid interface such that solidification is in the Y' direction and the container walls are at $X' = \pm L/2$. We consider a two dimensional problem (no Z'-dependence) and assume that all quantities are independent of time in the moving frame. The shape of the solid-liquid interface is denoted by $Y' = W'(X')$.

The solute concentration C' in the liquid satisfies the differential equation

$$\nabla'^2 C' + (V/D)(\partial C'/\partial Y') = 0, \qquad (1)$$

where D is the diffusion coefficient in the liquid (diffusion in the solid is neglected). The boundary conditions are

41

$$V[C'_I(k-1)] = D[(\partial C'/\partial Y')_I - (\partial C'/\partial X')_I(\partial W'/\partial X')], \qquad (2a)$$

$$C'(X',Y' \to \infty) = C'_\infty, \qquad (2b)$$

and

$$(\partial C'/\partial X') = 0 \quad \text{at} \quad X' = \pm L/2, \qquad (2c)$$

where the subscript I denotes evaluation at the solid-liquid interface, $k = C'_{SI}/C'_I$ is the partition coefficient (ratio of the solid solute concentration C'_S to the liquid solute concentration C' at the interface), which is assumed constant, and C'_∞ is the bulk solute concentration.

We introduce dimensionless variables $X = X'/L$, $Y = Y'/L$, $W = W'/L$, $C = C'/C'_\infty$, and $\beta = VL/D$; the above equations can then be written as

$$\nabla^2 C + \beta(\partial C/\partial Y) = 0, \qquad (3)$$

$$\beta C_I(k-1) = (\partial C/\partial Y)_I - (\partial C/\partial X)_I(\partial W/\partial X), \qquad (4a)$$

$$C(X,Y \to \infty) = 1, \qquad (4b)$$

$$(\partial C/\partial X) = 0 \quad \text{at} \quad X = \pm \tfrac{1}{2}. \qquad (4c)$$

In this form, it is clear that the concentration C depends on the dimensionless quantities β and k and the interface shape $Y = W(X)$.

For $W(X)$ independent of X, viz, $W(X) = W_0$ (a constant), the solution of Eqs. (3-4) is independent of X; we denote this solution by

$$C_0(Y) = 1 + [(1-k)/k]\exp[-\beta(Y-W_0)]. \qquad (5)$$

For numerical calculation, we introduce the function $U(X,Y)$ defined by

$$U(X,Y) = [C(X,Y) - C_0(Y)]\exp(\beta Y/2). \qquad (6)$$

In terms of $U(X,Y)$, the differential equations and boundary conditions are

$$\nabla^2 U - (\beta/2)^2 U = 0, \qquad (7)$$

$$(\partial U/\partial Y)_I + (\beta/2)(1-2k)U_I - (\partial U/\partial X)_I(\partial W/\partial X) =$$
$$\beta(k-1)\exp(\beta W/2)\{1-\exp[-\beta(W-W_0)]\}, \qquad (8a)$$

$$U(X, Y \to \infty) = 0, \qquad (8b)$$

$$(\partial U/\partial X) = 0 \quad \text{at} \quad X = \pm \tfrac{1}{2}. \qquad (8c)$$

Instead of using the boundary condition for $Y \to \infty$, Eq. (8b), directly in our computations, we shall obtain an equivalent condition at a finite value of Y, viz. Y_∞. Calculation of the volume integral of Eq. (3), and use of Green's theorem, Eq. (4a), and Eq. (4c) yields

$$\langle(\partial C/\partial Y) + \beta C\rangle_{Y=Y_\infty} = k\beta\langle C\rangle_I \qquad (9)$$

where $\langle \ \rangle$ indicates integration with respect to X from $X = -\tfrac{1}{2}$ to $\tfrac{1}{2}$. As Y_∞ approaches ∞, $(\partial C/\partial Y) \to 0$ and $C \to 1$ so that $k\langle C\rangle_I = 1$, which is a mathematical statement of solute conservation, viz, $\langle C'_s\rangle_I = C'_\infty$. We then choose Y_∞ sufficiently large that $C(X, Y_\infty)$ is nearly independent of X in which case Eq. (9) becomes approximately

$$(\partial C/\partial Y) + \beta C = \beta \quad \text{at} \quad Y = Y_\infty, \qquad (10)$$

which is a computationally efficient equivalent of Eq. (4b). Substitution of Eq. (6) into Eq. (10) then yields

$$(\partial U/\partial Y) + (\beta/2)U = 0 \quad \text{at} \quad Y = Y_\infty, \qquad (11)$$

which we use in place of Eq. (8b) for numerical computation.

3. ANALYTIC RESULTS

The concentration C depends on the interface shape W(X) and the parameters β and k. With appropriate restrictions on W(X), β, and k, it is possible to obtain analytic approximations for the concentration.

A. Small Deviations of the Interface from Planarity

For nearly planar interfaces, the perturbation methods of the theory of morphological stability allow calculation of the concentration [1]; we briefly review these results.

We assume that W(X) and $(\partial W/\partial X)$ are sufficiently small that second order terms in these quantities may be neglected. We write the interface shape as a Fourier series, viz,

$$W(X) = \delta(0) + \sum_{n=1}^{\infty} \delta(n)\cos(2n\pi X), \qquad (12)$$

where $\delta(n)$ is a Fourier coefficient and we have assumed that W(X) is a symmetric function, i.e., W(X) = W(-X). The interface concentration in the solid is

$$C_{SI} \cong 1-\beta(1-k)\sum_{n=1}^{\infty} \delta(n)\cos(2n\pi X)/\{1 + 2k/[g(n)-1]\}, \qquad (13)$$

where $g(n) = \{1 + (4\pi n/\beta)^2\}^{\frac{1}{2}}$. In deriving this equation we have assumed that $\{\frac{1}{2} + g(n)\}\{\beta[W(X) - \delta(0)]\} < <1$. If $2k/[g(1)-1] < < 1$, Eq. (13) has the simple form

$$C_{SI} \cong 1-\beta(1-k)[W(X)-\delta(0)] \qquad (14)$$

Previously [1], we evaluated Eq. (13) for [W(X)-δ(0)] quadratic in X; we will compare our numerical results with Eq. (13) in a later section of

44

this paper. We expect Eq. (13) to be a good approximation if β is small but its precise justification depends on the detailed conditions discussed above.

B.   Boundary Layer; $\beta >> 1$

When $\beta >> 1$, we can apply singular perturbation techniques to obtain an approximation for the concentration. We introduce new coordinates (ξ,η) such that $\xi = X$ and $\eta = \beta[Y-W(X)]$. The differential equation and boundary conditions can be written as

$$(\partial^2 C/\partial\eta^2)[1 + (\partial W/\partial\xi)^2] + (\partial C/\partial\eta) -$$
$$[2(\partial W/\partial\xi)(\partial^2 C/\partial\eta\partial\xi) + (\partial^2 W/\partial\xi^2)(\partial C/\partial\eta)]/\beta +$$
$$(\partial^2 C/\partial\xi^2)/\beta^2 = 0, \tag{15}$$

$$C(k-1) = (\partial C/\partial\eta)[1+(\partial W/\partial\xi)^2] - (\partial C/\partial\xi)(\partial W/\partial\xi)/\beta \quad \text{at} \quad \eta = 0, \tag{16a}$$

$$C(\xi,\eta \to \infty) = 1, \tag{16b}$$

$$(\partial C/\partial\xi) - \beta(\partial W/\partial\xi)(\partial C/\partial\eta) = 0 \quad \text{at} \quad \xi = \pm \tfrac{1}{2}. \tag{16c}$$

We proceed to expand C as a power series in $(1/\beta)$ and in Eqs. (15-16) equate coefficients of β^{-n}. To order β^{-2}, the interface concentration in the solid is

$$C_{SI} \cong 1 + [(1-k)/(k\beta)](\partial^2 W/\partial\xi^2) +$$
$$[(1-k)(1+2k)/(k^2\beta^2)][(\partial^2 W/\partial\xi^2)^2 + (\partial W/\partial\xi)(\partial^3 W/\partial\xi^3)], \tag{17}$$

where it has been necessary to assume that $(\partial W/\partial\xi) = (\partial^3 W/\partial\xi^3) = 0$ at $\xi = \pm \tfrac{1}{2}$ in order to satisfy Eq. (16c).

According to Eq. (17), $C_{SI} \to 1$ as $\beta \to \infty$ whereas according to Eq. (14), $C_{SI} \to 1$ as $\beta \to 0$. Evidently, therefore, the maximum deviation of C_{SI} from 1 occurs for some intermediate value of β and segregation due to a curved interface is minimal for both very large and very small

β. This maximum deviation for intermediate values of β is even consistent with Eq. (13) once the dependence of $g(n)$ on β is taken into account.

In order to better compare Eq. (17) with Eq. (13) and with subsequent numerical calculations, we·take $W(X) = \delta \cos (2\pi X)$ in Eq. (17) to obtain

$$C_{SI} \cong 1 - [(1-k)/k][4\pi^2 \delta/\beta] \cos (2\pi X)$$
$$+ [(1-k)/k][(1+2k)/k][4\pi^2 \delta/\beta]^2 \cos (4\pi X). \tag{18}$$

For $\beta >> 4\pi$ and also $\beta >> 2\pi k^{-\frac{1}{2}}$, Eq. (13) is in agreement with the linear term in δ in Eq.·(18), thus demonstrating a common region of validity of the two analytical approximations.

4. NUMERICAL CALCULATIONS AND RESULTS

We have calculated the solute distribution for the interface shape $W(X) = \delta \cos (2\pi X)$ for various values of the amplitude δ, for $k = 0.1$, 0.5, 2.0, and 10.0, and for $(\beta/4\pi) = 0.01$, 0.1, and 1.0. All numerical solutions of Eq. (7) with the boundary conditions given by Eqs. (8a, 8c, and 11) with $W_0 = 0$ were carried out with ELLPACK, a programming system for linear elliptic boundary value problems [2-3]. A value of $Y_\infty = 1.5$ was usually sufficiently large to yield $C(X, Y_\infty)$ independent of X and the domain was further restricted to $0 \leq X \leq \frac{1}{2}$ by symmetry. Two distinct methods were available to determine the concentration field. The first was a standard finite difference approximation [4] on a uniform rectangular grid (ELLPACK module 5-POINT STAR) while the second performed a Rayleigh-Ritz approximation on six-node triangular finite elements [5-6] with automatic user-controlled mesh grading (ELLPACK module 2DEPEP). The resulting systems of linear equations were solved by variants of Gaussian elimination in each case, the former using a widely distributed in-core sparse matrix solver [7] (ELLPACK modules YALE MIN DEG and YALE

46

SPARSE (DRV=T)) and the latter using the reverse Cuthill-McKee ordering for equations and unknowns to get a banded matrix and the frontal method to organize out-of-core storage.

Computations were performed in single precision on a Univac 1108 computer (8 decimal digits of precision). The finite element method was used for all cases; for a number of cases with $(\beta/4\pi) = 0.01$ and 0.1, good agreement was obtained between the finite difference and finite element calculations. A computer solution was accepted provided solute was conserved (to about three digit accuracy) and no severe oscillations were present. For a typical computation a 40 x 40 grid was used for the finite difference program and 400 triangles for the finite element program, yielding about 1200 and 850 unknowns, respectively. Separate computations were performed to help assess the effects of truncation and rounding errors; the latter were done by comparing results with selected runs made on a CDC 6500 computer (14 decimal digits of precision).

Further confidence in the numerical results was obtained by assessing the performance of the codes on a slightly different problem. The function $\hat{U} = A \exp \{\beta[W(X)-\tfrac{1}{2}Y]\} + (B-A) \exp (-\tfrac{1}{2}\beta Y)$,

where $A = 2(1-k)/\{2k-1 + [1+(4\pi/\beta)^2]^{\frac{1}{2}}\}$,

$B = [(1-k-kA)/k][-1+1/I_0(\beta\delta)]$,

and, I_0 is a modified Bessel function, has the same qualitative behavior expected of U, satisfies Eqs. (8c) and (11) exactly, and satisfies Eqs. (7) and (8a) with different inhomogeneous terms. When solving for $\hat{U}$ with $k=0.1$, $W(X) = 0.4 \cos (2\pi X)$ and $Y_\infty = 1.5$, the finite element program yielded errors in the value of $C_{SI}(\tfrac{1}{2})$ of 0.01, 0.1, and 2.0 percent for $(\beta/4\pi) = 0.01$, 0.1, and 1.0 respectively. The errors in

47

overall solute conservation are often comparable or somewhat smaller than those in the local solute concentration.

In Table 1, for various values of k, β, and δ, we give the interface concentration $C_{SI}(X) = kC_I(X)$ in the solid at $X = 0$ and $\frac{1}{2}$, i.e., at the maximum and minimum of the interface position. The average interface concentration $<C_{SI}> = 1$ in the solid; the numerically computed values of this quantity are given in Table 1 and provided an indication of the accuracy of the calculations. The values of $C_{SI}(X)$ calculated from Eq. (13), which we denote by $C_{SIA}(X)$, are also given in Table 1 for $X = 0$ and $\frac{1}{2}$. Comparison of C_{SIA} with C_{SI} indicates excellent agreement for small values of β.

In Figs. 2-5, we plot $C_{SI}(\frac{1}{2})$ and $C_{SI}(0)$ as a function of δ for $k = 0.1$, 0.5, 2.0, and 10.0, respectively. If Eq. (13) is a good approximation, we expect $C_{SI}(\frac{1}{2})$ and $C_{SI}(0)$ to be linear functions of δ and to be symmetric about $C_{SI} = 1$. It is seen that this is the case for β small; however, there is increasing deviation from this behavior as β increases. We know from Eq. (18) that C_{SI} approaches 1 as β becomes very large; this is consistent with our numerical calculations as is apparent from Fig. (5) for $k=10$. Unfortunately the values of β needed to make Eq. (18) a good approximation are so large, except for extremely small values of δ, that numerical computations for these values of β have not been practical.

In Fig. 6 for $W(X) = 0.4 \cos 2\pi X$ and $k = 0.5$, we show the interface concentration in the solid C_{SI} as a function of X for $(\beta/4\pi) = 0.01$, 0.1, and 1.0, while in Fig. 7 for $(\beta/4\pi) = 1.0$ and $k = 0.1$, we plot $C_{SI}(X)$ for $\delta=0.05$, 0.1, 0.2, and 0.4. With increasing values of β and δ, the interface concentration becomes almost independent of X for $X \leq 0.25$, and then changes rapidly for $0.25 \leq X \leq 0.5$.

48

We previously obtained an approximate expression (Eq. (14) of reference 1) for $[C_{SI}(\frac{1}{2}) - C_{SI}(0)]$ for an interface of shape $W(X) = (s/12)(1-12X^2)$, where s is the magnitude of the maximum interface slope, viz., $s = |(\partial W/\partial X)|$ at $X = \pm \frac{1}{2}$. Finite element calculations have shown the validity of our approximate expression for sufficiently small s (small deviations from planarity). For example, with k = 0.001 the relative error between the numerical and approximate results is less than four percent for s less than 1/16, 1/2, and 4 with $(\beta/4\pi)$ = 1.0, 0.1, and 0.01, respectively.

5. CONCLUSIONS

We have calculated the lateral solute segregation consistent with a non-planar interface of assumed shape by means of two analytical expressions, valid in limiting cases, and by numerical techniques.

For a fixed interface shape, the segregation depends on the distribution coefficient k and the parameter $\beta = VL/D$. For both very small β and very large β, Eqs. (13) and (17) show that the segregation tends to zero. Maximum segregation occurs at an intermediate value of β that depends on k. This is illustrated in Fig. 8 where we plot $|[C_{SI}(\frac{1}{2}) - C_{SI}(0)]/\delta|$ for an interface of the form $W(X) = \delta \cos(2\pi X)$ as a function of β for k = 0.1, 0.5, 2.0, and 10.0 according to Eq. (13). Although Eq. (13) has limited validity, as discussed previously, the fact that maximum segregation occurs at intermediate values of β is evident. The limiting cases correspond to very thick and very thin solute boundary layers, respectively. Changes of interface topography that are small compared to the boundary layer thickness have a proportionally small effect on segregation; in the extreme opposite case, a

49

very thin boundary layer essentially bends to conform to the shape of an interface whose radius of curvature is large compared to the boundary layer thickness.

In the limit of both very small and very large β, Eqs. (13) and (18) show that segregation is proportional to the distance that the interface departs from planarity. For intermediate values of β, this is not true and the results of our numerical calculations, displayed in Figs. 2-5, show a non-linear increase with δ except for the case $(\beta/4\pi)$ ≈ 0.01 for which there is good linearity even to large values of δ. It is rather amazing that Eq. (13) appears to agree reasonably with the numerical results for small β even for very large values of δ. The non-linear increase of segregation with δ for intermediate values of β means, for instance, that a sinusoidal interface shape will result in a non-sinusoidal interface segregation profile such as is evident in Figs. 6-7 for $(\beta/4\pi) = 1$. In particular, the segregation profiles are nearly flat near the hills (projections of the solid into the liquid) and change abruptly in the valleys (projections of the liquid into the solid). This behavior is true for both $k < 1$ and $k > 1$ and is probably due to the exponential character of the concentration field near the solid-liquid interface. For a cellular structure, for example, one would expect little variation of concentration near the cell tip but pronounced segregation at the grooves.

For a cellular interface, Flemings [8] has given a formula [Eq. (3-20)] for lateral segregation under the assumption of a temperature field linear in Y and a concentration field that is independent of X in the liquid. These conditions, when combined with the assumption of

50

local equilibrium and the conservation of solute, imply a definite interface shape. It would be inappropriate to compare our results with those of Flemings unless we choose an interface shape consistent with his model. This has not been done since, as stated in the introduction, we have made no attempt to reconcile our shape with any preconceived thermal field. Interface shapes consistent with various thermal fields have been investigated by Ettouney and Brown [9] using finite element techniques.

ACKNOWLEDGMENTS

REFERENCES

1. S. R. Coriell and R. F. Sekerka, J. Crystal Growth 46 (1979) 479.

2. J. R. Rice, in: Mathematical Software III, Ed. J. R. Rice (Academic Press, New York, 1977) p. 319.

3. J. R. Rice, Comp. Sci. Dept. Report CSD-TR 306, Purdue Univ., Lafayette, IN, 1979.

4. G. E. Forsythe and W. R. Wasow, Finite Difference Methods for Partial Differential Equations (John Wiley, New York, 1960).

5. G. Strang and G. J. Fix, An Analysis of the Finite Element Method (Prentice-Hall, Englewood Cliffs, NJ, 1973).

6. G. Sewell, in: Advances in Computer Methods for Partial Differential Equations III, Eds. R. Vichnevetsky and R. S. Stepleman (IMACS, New Brunswick, NJ, 1979) p. 8.

7. S. C. Eisenstat, M. C. Gursky, M. H. Schultz, and A. H. Sherman, Dept. of Comp. Sci. Report 114, Yale Univ., New Haven, CT, 1977.

8. M. C. Flemings, Solidification Processing (McGraw-Hill, New York, 1974).

9. H. M. Ettouney and R. A. Brown, 73rd Annual Meeting of AIChE, Nov. 1980, Chicago.

TABLE 1

Solute Segregation for the Solid-Liquid Interface Shape
$W(X) = \delta \cos(2\pi X)$

k	$(\beta/4\pi)$	δ	$<c_{SI}>$	$c_{SI}(0)$	$c_{SIA}(0)$	$c_{SI}(\frac{1}{2})$	$c_{SIA}(\frac{1}{2})$
0.1	0.01	0.1	1.000	0.989	0.989	1.011	1.011
		0.2	1.000	0.978	0.977	1.023	1.023
		0.4	1.001	0.956	0.955	1.046	1.045
		0.6	1.000	0.934	0.932	1.069	1.068
		1.0	1.001	0.892	0.887	1.116	1.113
	0.1	0.1	1.000	0.893	0.893	1.114	1.107
		0.2	1.000	0.795	0.787	1.233	1.213
		0.4	1.001	0.625	0.574	1.479	1.426
	1.0	0.05	1.000	0.680	0.619	1.429	1.381
		0.1	1.000	0.481	0.237	1.906	1.763
		0.2	1.002	0.312	-0.525	2.804	2.525
		0.4	1.011	0.23	-2.051	4.19	4.051
0.5	0.01	0.1	1.000	0.994	0.994	1.006	1.006
		0.2	1.000	0.988	0.988	1.013	1.012
		0.4	1.000	0.976	0.975	1.025	1.025
	0.1	0.1	1.000	0.893	0.893	1.114	1.107
		0.2	1.000	0.795	0.787	1.233	1.213
		0.4	1.001	0.625	0.574	1.479	1.426
	1.0	0.05	1.000	0.920	0.908	1.103	1.092
		0.1	1.000	0.863	0.816	1.222	1.184
		0.2	1.000	0.793	0.632	1.465	1.368
		0.4	1.001	0.729	0.264	1.861	1.736
2	0.01	0.1	1.000	1.012	1.012	0.988	0.988
		0.2	1.000	1.024	1.024	0.976	0.976
		0.4	1.000	1.046	1.048	0.953	0.952
	0.1	0.1	1.000	1.083	1.087	0.913	0.913
		0.2	1.000	1.153	1.174	0.833	0.826
		0.4	1.000	1.258	1.349	0.709	0.651
	1.0	0.05	1.000	1.053	1.059	0.935	0.941
		0.1	1.000	1.094	1.118	0.859	0.882
		0.2	1.000	1.154	1.236	0.710	0.764
10	0.01	0.1	1.000	1.093	1.094	0.907	0.906
		0.2	1.000	1.179	1.188	0.822	0.812
		0.4	1.000	1.332	1.376	0.680	0.624
	0.1	0.1	1.000	1.326	1.352	0.660	0.648
		0.2	1.000	1.582	1.705	0.408	0.295
		0.4	1.001	1.948	2.409	0.164	-0.409
	1.0	0.05	1.000	1.105	1.115	0.874	0.885
		0.1	1.000	1.189	1.229	0.732	0.771

FIGURE CAPTIONS

1. Geometry associated with unidirectional solidification with a curved solid-liquid interface. The sample is of width L and the origin of X' is located such that the sample walls are at X' = ± L/2.

2. The solute concentration C_{SI} in the solid at the solid-liquid interface at X = ½ (values greater than 1) and at X = 0 (values less than 1) as a function of the amplitude δ of a sinusoidal interface shape, W(X) = δ cos (2πX), for a distribution coefficient k = 0.1 and for (β/4π) = 0.01, 0.1, and 1.0.

3. The solute concentration C_{SI} in the solid at the solid-liquid interface at X = ½ (values greater than 1) and at X = 0 (values less than 1) as a function of the amplitude δ of a sinusoidal interface shape, W(X) = δ cos (2πX), for a distribution coefficient k = 0.5 and for (β/4π) = 0.01, 0.1, and 1.0.

4. The solute concentration C_{SI} in the solid at the solid-liquid interface at X = 0 (values greater than 1) and at X = ½ (values less than 1) as a function of the amplitude δ of a sinusoidal interface shape, W(X) = δ cos (2πX), for a distribution coefficient k = 2 and for (β/4π) = 0.01, 0.1, and 1.0.

5. The solute concentration C_{SI} in the solid at the solid-liquid interface at X = 0 (values greater than 1) and at X = ½ (values less than 1) as a function of the amplitude δ of a sinusoidal interface shape, W(X) = δ cos (2πX), for a distribution coefficient k = 10 and for (β/4π) = 0.01, 0.1, and 1.0.

6. The solute concentration C_{SI} in the solid at the solid-liquid interface of shape W(X) = 0.4 cos (2πX) as a function of position X for k = 0.5 and (β/4π) = 0.01, 0.1, and 1.0.

7. The solute concentration C_{SI} in the solid at a solid-liquid interface of shape $W(X) = \delta \cos (2\pi X)$ as a function of position X for $k = 0.1$, $(\beta/4\pi) = 1.0$, and $\delta = 0.05$, 0.1, 0.2, and 0.4.

8. The quantity, $\Delta C/\delta \equiv |[C_{SI}(\tfrac{1}{2}) - C_{SI}(0)]/\delta|$, as a function of β for various values of the distribution coefficient k as calculated from Eq. (13) for an interface of shape $W(X) = \delta\cos(2\pi X)$.

$W(X) = \delta \cos (2\pi X)$
$k = 0.1$

$\beta = 4\pi$

$\beta = 0.4\pi$

$\beta = 0.04\pi$

$\beta = 0.04\pi$

$\beta = 0.4\pi$

$\beta = 4\pi$

$C_{S1}(\tfrac{1}{2})$

$C_{S1}(0)$

δ

$W(X) = \delta \cos(2\pi X)$

$k = 0.5$

$\beta = 4\pi$

$\beta = 0.4\pi$

$\beta = 0.04\pi$

$\beta = 0.04\pi$

$\beta = 0.4\pi$

$\beta = 4\pi$

$C_{SI}(1/2)$

$C_{SI}(0)$

δ

58

$$W(X) = \delta \cos (2\pi X)$$

$$k = 2$$

$\beta = 4\pi$ $\beta = 0.4\pi$

$\beta = 0.04\pi$

$\beta = 0.04\pi$

$\beta = 4\pi$ $\beta = 0.4\pi$

$W(X) = \delta \cos(2\pi X)$
$k = 10$

$C_{SI}(0)$

$C_{SI}(1/2)$

$\beta = 0.4\,\pi$

$\beta = 0.04\,\pi$

$\beta = 4\,\pi$

$\beta = 4\,\pi$

$\beta = 0.04\,\pi$

$\beta = 0.4\,\pi$

δ

$W(X) = 0.4 \cos(2\pi X)$

$k = 0.5$

$W(X) = \delta \cos(2\pi X)$
$k = 0.1$
$\beta = 4\pi$

$$W(X) = \delta\cos(2\pi X)$$